Transp Porous Med (2012) 94:505–524
DOI 10.1007/s11242-012-9941-z

Improving the Estimations of Petrophysical Transport Behavior of Carbonate Rocks Using a Dual Pore Network Approach Combined with Computed Microtomography

D. Bauer · S. Youssef · M. Fleury · S. Bekri · E. Rosenberg · O. Vizika

Received: 5 May 2011 / Accepted: 6 January 2012 / Published online: 27 January 2012

Abstract Due to the intricate structure of carbonate rocks, relationships between porosity or saturation and petrophysical transport properties classically used for reservoir estimation and recovery strategies are either very complex or nonexistent. Thus, further understanding of the influence of the rock structure on the petrophysical transport properties becomes relevant. We therefore present a Dual Pore Network approach (D-PNM) applied to μ-CT images of bimodal porous media. The major advantage of this method lies in the fact that it takes into account the real architecture of the connected macropore network as well as the microporosity unresolved by μ-CT imaging. Whereas governing equations are solved in each individual macropore, transport behavior of microporosity is simulated by average quantities. Thus, D-PNM is particularly suited for the investigation of carbonate rocks, characterized by broad pore size distributions. We describe the principles of the image acquisition and network extraction procedure and the governing equations of D-PNM. The model is tested on three carbonate samples, two outcrop, and one reservoir carbonate. Calculated petrophysical transport properties are compared to experimental data and we show that D-PNM correctly reproduces conventional as well as unconventional electrical transport behavior. A major restriction of D-PNM is the requirement of a connected macropore network, that is, especially in the case of carbonates, not always available. Solutions to that are presented.

Keywords Dual Pore Network Model · Computed Microtomography · Petrophysical transport properties · Carbonate rocks

List of Symbols

- α Half angle of the polygon describing the throat or pore
- θ Contact angle
- ρ Radius of the curvature of the oil–water interface, depending on the applied pressure

D. Bauer · S. Youssef (✉) · M. Fleury · S. Bekri · E. Rosenberg · O. Vizika
IFP Energies nouvelles, 1 et 4 av. Bois-Préau, 92852 Rueil-Malmaison, France
e-mail: souhail.youssef@ifpen.fr

μ	Fluid viscosity
σ_w	Electrical conductivity of bulk water
ϕ_{img}	Global porosity of the 3D image
ϕ_{mi}	Mean porosity of the microporous phase
A	Cross-section of the network
A_{con}	Cross-section of the cuboid perpendicular to the flow direction
A_w	Area of the wetting phase occupying the corners of the pores and throats
$A_{w,s}$	Cross-sectional area occupied by the water phase
FF	Formation factor
FF_{mi}	Formation factor of the microporous phase
F_{ma}	Fraction of the macroporous phase (resolved porosity)
F_{mi}	Fraction of the microporous phase
F_{surf}	Fraction of the macropore surface in contact with the microporous phase
g_h	Hydraulic conductance
g_e	Electrical conductance
G_m	Mean grey level of the image
G_s	Peak grey levels of the solid phase
G_v	Peak grey level of the void phase
i, j	Pore labels
K	Permeability
K_r	Relative permeability
L	Length of the network
I_{ij}	Electrical current
l_{con}	Length of the microporous cuboid lining the macropore segments along the flow direction
l_{ff}	Equivalent electrical throat length
l_h	Equivalent hydraulic throat length
m	Cementation exponent
m_{mi}	Cementation exponent of the microporous phase
n	Saturation exponent
n_c	Number of corners of the pore or throat polygon
n_{mi}	Cementation exponent of the microporous phase
N_{ma}	Number of voxels of the resolved porosity
N_{img}	Total number of voxels in the image
N_{mi}	Number of voxels of the microporous phase
N_{seg}	Number of segments
P	Pressure
P_c	Capillary pressure
Q	Macroscopic flow rate
q_{ij}	Flow rate in the throat between pore i and j
p_{seg}	Percentage of pore segments with microporosity acting in parallel
r_h	Hydraulic radius
R_0	Resistivity of the saturated porous media
RI	Resistivity index
R_t	Resistivity of the partially saturated porous media
S_w	Water saturation
U_i, U_j	Electrical potential in the neighboring pores

1 Introduction

Carbonate fields are expected to dominate oil production during the next years, as they present over 50% of the actual world reserves. Thus, meaningful reservoir estimations become crucial. However, in this type of rock, relationships between porosity or saturation and petrophysical transport properties classically used for reservoir estimation and recovery strategies are either very complex or nonexistent. This can be illustrated by means of Archie's law relating the water saturation (S_w) to the electrical resistivity R_t. One of the steps in the estimation procedure is the determination of the resistivity index curve ($RI = R_t/R_0$, R_0: resistivity at full saturation) relating RI to S_w. Conventionally, in the absence of core measurements, $RI = S_w^{-n}$ and the saturation exponent n is taken equal to 2 based on historical measurements performed on sandstones (Archie 1942; Schlumberger 1987). However, in some cases the saturation exponent n can largely deviate from 2, or become non linear on a log–log scale (Focke and Munn 1987; Bouvier and Maquignon 1991; Fleury 2002; Padhy et al. 2006).

This unconventional non-Archie behavior of carbonates might be explained by their bimodal pore size distributions which are generally very large, ranging from tenth of nm to mm. But also by the topology of the pore space that is very complex and defers from one reservoir to the other, as it strongly depends on the individual carbonate formation and alteration process. Thus, further understanding of the influence of the rock structure on the petrophysical transport properties becomes relevant.

Given the economic consequences, the need for efficient models taking into account the complex rock structure as well as the physics of the two-phase flow at the pore scale cannot be ignored. Important advances in combining computed microtomography (μ-CT) imaging with different modeling techniques (finite elements and volumes, random walk) were achieved (Bekri et al. 2003; Knackstedt et al. 2007; Han et al. 2009). In these articles, governing equations are directly solved in the 3D pore space obtained from segmented images. The objective of this study is to continue these efforts by combining μ-CT imaging with a Dual Pore Network approach (D-PNM) that allows the investigation of relatively large volumes at a reasonable computation time.

Pore Network Models (PNM) (Fatt 1956; Payatakes et al. 1973; Lenormand et al. 1983; Diaz et al. 1987; Blunt and King 1990; Laroche et al. 1999) represent the pore space by a 3D network of interconnected pores and throats of simple geometry. Flow governing equations are obtained from Poiseuilles law. To accurately describe the flow conductance, Poiseuilles radius and length should correctly reflect the real pore and throat shape (Oren et al. 1998; Patzek and Silin 2001; Sholokhova et al. 2009). The development of PNM based on real rock structures has made significant advances with the advent of Synchrotron μ-CT generating 3D data sets at the micron scale (Coles et al. 1996; Lindquist et al. 2000; Knackstedt et al. 2004). Fluid transport calculations initially based upon reconstructions from 2D thin sections (Adler and Thovert 1998) or upon numerical reconstructions (Oren et al. 1998; Valvatne and Blunt 2003) have been extended to 3D μ-CT images. Recently, interdisciplinary teams have contributed to improve topological partitions of the pore space and fluid transport predictions based on these μ-CT data (Arns et al. 2004a,b; Bauget et al. 2005; Knackstedt et al. 2006; Olafuyi et al. 2008).

In this article, we present a D-PNM (Ioannidis and Chatzis 2000; Bekri et al. 2002; Moctezuma-Berthier et al. 2003; Bekri et al. 2005; Youssef et al. 2008) applied to μ-CT images of bimodal porous media.

The principal interest of this model is based on the fact that it allows the simulation of flow in the macropore network obtained from the μ-CT images and to take into account the

influence of the microporosity, unresolved by μ-CT imaging, on the macroscopic transport by means of its average quantities.

In carbonates, a fraction of the pore space generally remains unresolved by the current standard μ-CT equipments, motivating the investigation of the latter rocks by D-PNM.

In this article, we first introduce the image acquisition and network extraction procedure. Then, we present the governing equation of the single and the D-PNM. The latter is then evaluated by calculating the petrophysical transport properties of three carbonate samples, two outcrops, and one reservoir carbonate. Results are compared to experimental data. We show that D-PNM estimates conventional as well as unconventional transport behavior.

A major disadvantage of D-PNM lies in the fact that it is based on a connected macropore network. Unfortunately, due to their pore size distribution this is not always the case when investigating carbonates. Solutions to the latter difficulty will be presented.

2 Materials and Methods

2.1 Sample Characteristics

Three carbonate samples each one characterized by a bimodal pore size distribution were considered in this article: one reservoir carbonate and two outcrop carbonates (Estaillades and Lavoux). The experimental petrophysical properties (permeability: K, porosity: ϕ, formation factor: FF, mercury intrusion (MICP) data (pore access diameter), multiphase transport properties: K_r and RI) are summarized in Table 1. Porosities are ranging from 20 to 30% and formation factors from 13 to 50. Permeability values between 23 and 273 mD can be observed.

Pore access diameter distributions of the samples obtained from mercury intrusion show a bimodal distribution. The minimum between the two peaks stands for the limit between micro- and macroporosity. Thus, the minimal pore access diameter (d_{am}) of the macropores is given by the abscissa of the inter-peak minimum. Considering the outcrop samples, $d_{am} \sim 3\,\mu m$, however, it is lower for the reservoir sample ($\sim 0.5\,\mu m$). In addition, it can be seen from the mercury intrusion data that, in the Estaillade and the reservoir carbonate, most of the porosity is concentrated in the macroporosity. In contrast to that the Lavoux carbonate contains an abundant microporosity.

Multiphase transport experiments were conducted on samples with 40 mm in diameter and 30 mm in length. Resistivity index measurements were performed on the Estaillades and Lavoux samples whereas the relative permeabilities of the reservoir carbonate were measured.

2.2 Experiments: Multiphase Transport Properties

2.2.1 Electrical Transport Properties

Electrical transport properties of a porous media are defined by the formation factor FF, given by:

$$\mathrm{FF} = \frac{R_0}{R_w}, \tag{1}$$

where R_w is the resistivity of the saturating fluid and R_0 the resistivity at full saturation, and by the resistivity index

Table 1 Measured petrophysical properties of the studied samples, PV: pore volume, distribution: pore access diameter distribution

	Mercury injection data	Multiphase transport properties
Estaillade carbonate ϕ=24.7%, FF=24, K=273 mD	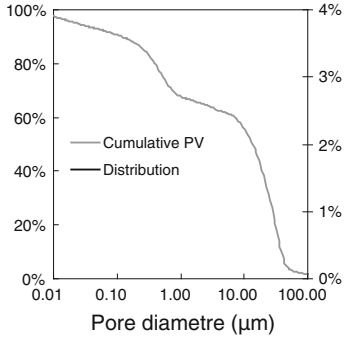	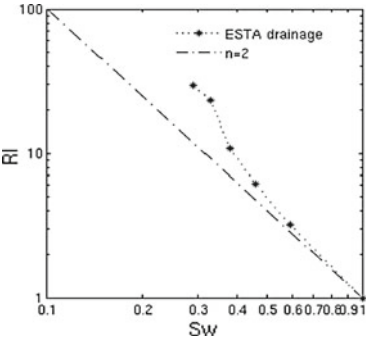
Lavoux carbonate ϕ= 28.7 %, FF=13, K = 90 mD	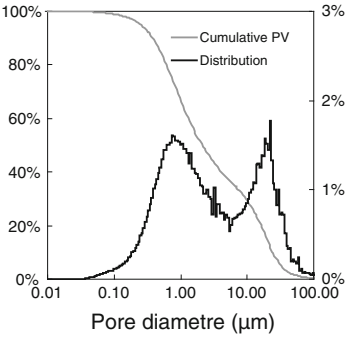	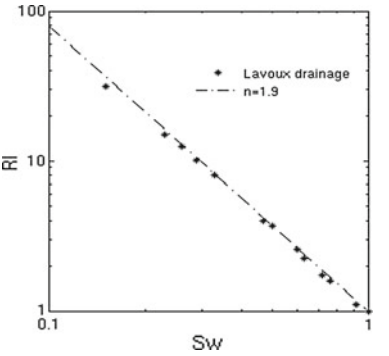
reservoir carbonate ϕ=20.6%, FF=50, K=23 mD	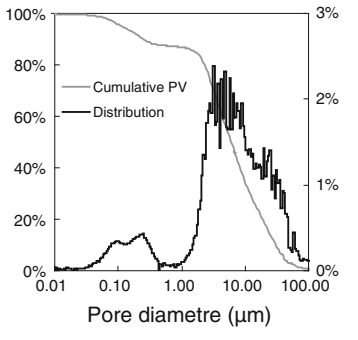	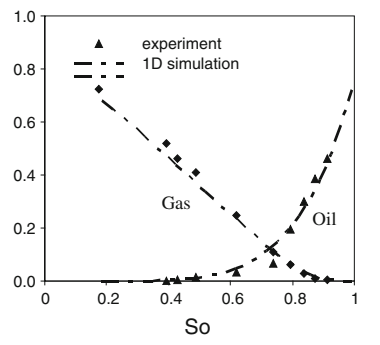

$$\mathrm{RI} = \frac{R_\mathrm{t}}{R_0} \tag{2}$$

relating the electrical resistivity R_t of the partially saturated porous media to the wetting phase saturation S_w.

Commonly, the electric multiphase transport properties are measured in air–brine systems. Whereas the formation factor is obtained at complete brine saturation, RI measurements are done at different saturation states obtained by horizontal centrifugation. After each centrifugation period, the amount of brine is measured by weighting and the electrical resistance is determined using a four electrode configuration. The RI is then obtained from the ratio of the resistance at a given saturation to the resistance at complete saturation. The experimental error of the resistance measurement is estimated to about 1% whereas the one of the saturation corresponds to 1 saturation unit. More information on RI measurements can be found in Fleury (1998) and Han et al. (2009).

Experimental results are shown in Table 1. As can be seen, the RI–S_w curve of the Estaillades carbonate during drainage exhibits a non-Archie behavior. The curve shows a positive deviation when the water saturation is below 40%. At the opposite, the RI–S_w curve of the Lavoux carbonate containing an abundant microporosity, follows almost perfectly Archie's law with an exponent value nearby 1.9.

2.2.2 Relative Permeabilities

Relative permeabilities are defined as:

$$K_{r\alpha} = K_\alpha (S) / K, \tag{3}$$

where $K_{r\alpha}(S)$ is the relative permeability of the phase α at the saturation state S and $K_\alpha(S)$ the effective permeability. K is the intrinsic permeability of the porous media.

Relative permeabilities are usually determined from flow experiments performed on core samples using either the unsteady- or the steady-state method. In both methods, samples are first saturated by fluid 1. Then, fluid 2 is either solely (unsteady-state) or simultaneously with fluid 2 injected. For this study, a standard steady-state experiment was conducted on the reservoir carbonate sample. Nitrogen and oil were used to avoid wettability effects and salt precipitation related to drying. The two fluids were simultaneously injected and the gas–oil flow rate ratio was increased at each step while monitoring the differential pressure for each fluid. This allows the gas saturation to increase. Saturation changes were monitored by CT scan. Relative permeabilities can then be directly calculated, at given saturation levels, from the acquired individual flow rates and pressure drops using Darcy's law if neglecting capillary effects. Nevertheless, due to the latter, the saturation distribution in the sample was non-uniform which can imply a different pressure drop in each phase. To consider this effect, gas/oil relative permeability curves were additionally derived by history matching of the experimental data with 1D numerical simulations. Gas/oil capillary pressure curves were obtained from the mercury porosimetry curve using the Leverett function. A zero capillary pressure boundary condition was applied at the outlet of the core to reproduce the experimental conditions. Relative permeability curves (cf. Table 1) were adjusted until a good match was obtained for water/gas production and pressure profile.

An error analysis for relative permeability was performed. The errors result from different aspects: porosity, saturation, absolute permeability, flow rates, and differential pressures measurements. The total error of the experience was estimated to 20%.

The experimental error of the absolute permeability measurement is about 6%.

2.2.3 Image Acquisition

The μ-CT equipment is a Nanotom from PHOENIX X-Ray. Common acquisition parameters for rock analysis are the following: 5 mm diameter sample, pixel size 3 μm (corresponding to

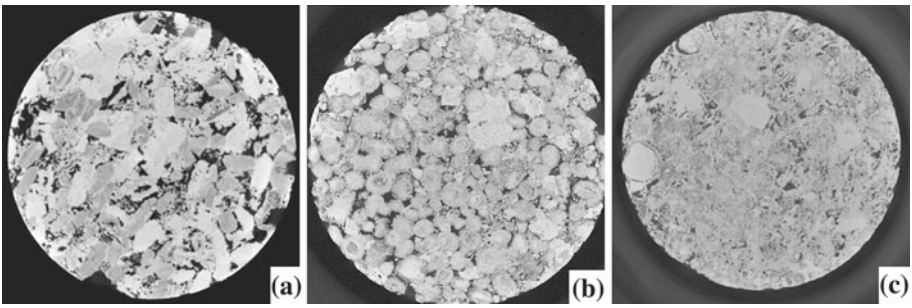

Fig. 1 X-Ray density maps of Estaillade carbonate (**a**), lavoux carbonate (**b**), and reservoir carbonate (**c**) slice extracted from 2, 000^3 voxel volumes at 3 μm resolution

the highest possible resolution for this sample size), 2, 300^2 field of view. To optimize image quality, the following set up conditions were used: high number of projections (3,600) to reduce noise and a 0.5 mm Cu filter to limit the outbreak of ring artifacts and beam hardening effects. Samples were imaged according to this optimal set up. For each scan a volume of $1,000^3$ voxels was reconstructed and converted into an 8 bit grey level image. Figure 1 shows slices extracted from the reconstructed volumes. Three phases can be distinguished: macroporosity (dark grey), the microporous phase (intermediate grey level), and the solid phase (bright grains). Although all samples show a bimodal pore size distribution, their topology is very distinct. Major difference lies in the connectivity of the microporous phase. Whereas the latter seems well connected in the Lavoux and the reservoir carbonate, connectivity of the microporous phase of the Estaillades carbonate is not obvious.

3 Modelling of Rock Properties

3.1 Pore Space and Parameter Extraction

3.1.1 Three Phase Segmentation

Image segmentation is a crucial step in image analysis. It aims to separate the different phases present in the raw image by assigning to each voxel of the image the corresponding phase depending on its grey level. In bimodal pore structure samples, we aim to correctly separate the microporous phase, the macropores and the solid phase. Please note that, for three-phase segmentation of μ-CT images, the limit between micro- and macropores is given by the μ-CT image resolution (3 μm) and not by the minimal pore access diameter d_{am} of the macropores.

To eliminate noise, raw images (cf. Fig. 2a) were previously filtered by assigning to each voxel the average grey value of its 5^3 neighbors (cf. Fig. 2b). Filtering led to an enhanced contrast and a better separation of the grey level peaks in the histograms (cf. Fig. 2e). The composite image of the 3D-phase distribution results then from the application of thresholds th1 and th2 (cf. Fig. 2c). The resulting image still contains some artifacts due to phase transition between the void space and the solid phase (grey level of the interface is of the same order of magnitude as the one of the microporous phase). This artifact is corrected by morphological operations (Caty et al. 2008) as growing, shrinking, and smoothing (cf. Fig. 2d).

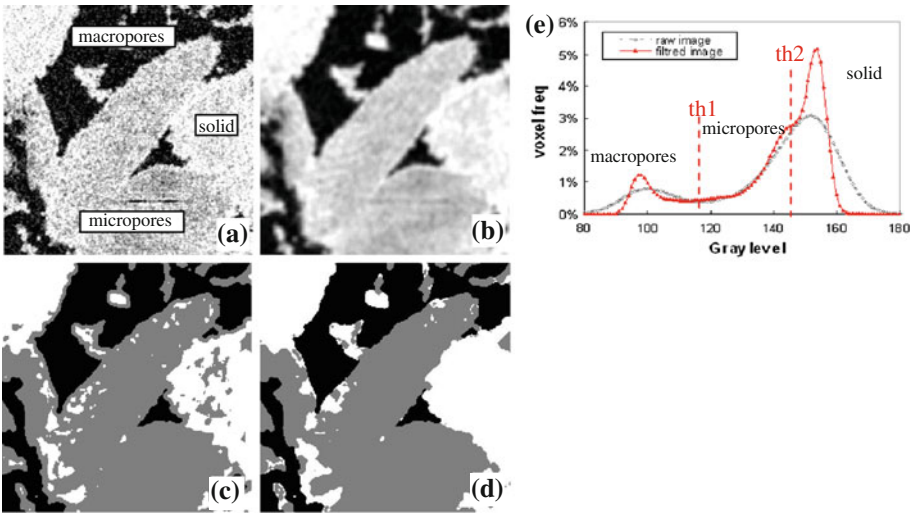

Fig. 2 Three-phase segmentation sequence: **a** 8-bit grey level raw image, **b** filtered image, **c** resulting composite image after applying thresholds th1 and th2, **d** final three-phase image after morphological operation, and **e** grey level histogram

3.1.2 Porosity Data and Phase Fractions

In monomineral rocks, porosity can be obtained from the grey level histogram before the segmentation step based on the Beer–Lambert law. In virtue of the latter, when X-ray penetrates through a material, its attenuation is a function of its atomic number and densities and the X-ray energies. Beer–Lambert law is given by $N_t = N_i e^{\mu x}$, where μ is the material's linear attenuation coefficient, N_t and N_i are the initial and final X-ray intensity and x is the length of the X-ray path. Thus, after reconstruction of the 3D image, we obtain a map of the local attenuation coefficients of the material. For constant energy in the photoelectric domain (energy below 200 KeV), as it is the case in this study, the following linear expression is valid: $\mu = \mu_0 Z^4 \rho$, where ρ is the local density of the sample, μ_0 a scale factor for the reconstruction process that depends on the X-ray energy and the acquisition geometry, and Z the material atomic number.

As carbonates are monomineral rocks, the hypothesis of a constant atomic number in the sample is valid. Thus, the local grey level of the image, that is proportional to the attenuation, becomes a linear function of the local density and therefore of the local porosity. Then, we consider that the grey level of the void space corresponds to a porosity of 1 and the one of the solid phase to a porosity of 0. Global porosity of the 3D image then becomes

$$\phi_{\text{img}} = (G_s - G_m)/(G_s - G_v), \tag{4}$$

where G_m represents the mean grey level of the image and G_v and G_s correspond to the grey levels of the maxima of the void and solid phase in the histogram. It is to be noticed that the mean filter does not affect the mean grey level G_m as it is a local averaging procedure.

We then extract the phase fractions $F_{ma} = N_{ma}/N_{img} = \phi_{ma}$ and $F_{mi} = N_{mi}/N_{img}$ from the composite image, where F_{ma}, F_{mi}, N_{ma}, N_{mi}, and N_{img} are, respectively, the resolved porosity fraction, the microporous phase fraction, the number of voxels of the resolved porosity, the number of voxels of the microporous phase, and the total number of voxels in the image. Using the above-mentioned phase fractions mean porosity (ϕ_{mi}) of the microporous phase becomes

$$\phi_{\mathrm{mi}} = \left(\phi_{\mathrm{img}} - F_{\mathrm{ma}}\right) / F_{\mathrm{mi}}. \tag{5}$$

Finally, we determine the fraction of the surface of macropores in contact with the microporous phase (F_{surf}). This is done by generating triangulated surfaces representing the boundaries between the different phases from the composite image.

3.1.3 Equivalent Pore Network

The pore network extraction methodology captures the resolved pore space of the rocks to partition it into individual pore volumes separated by throat surfaces. The extraction is processed in three steps: skeletonisation, pore space partitioning, and parameter calculation. The skeleton algorithm applied to the binary image is a hybrid algorithm combining thinning and distance map-based techniques called Distance Ordered Homotopic Thinning (Pudney 1998). Pores are individualized and characterized by their volumes. The pore volume intersections define the throat surfaces. Despite having a defined length, which will be used for the conductance calculation, throats have zero volume. Figure 3 shows the different steps of the pore space and network extraction procedure.

Pore network modeling requires a connected macropore network; isolated clusters are not taken into account by the model equations. We have seen in Sect. 2.1 that d_{am} of the outcrop samples are of the order of the μ-CT resolution. In this case, the extracted macropore network is automatically connected. In contrast, d_{am} of the reservoir sample is slightly smaller than the μ-CT resolution, leading to a large number of isolated clusters. However, as d_{am} is only slightly smaller than the μ-CT resolution we benefit from the heterogeneity of the sample. Thus, a large volume was investigated until a subvolume with a connected macropore network was found.

Table 2 summarizes parameters extracted from the binary images. Mercury intrusion (MICP) data is added for comparison. To obtain from MICP data porosity corresponding to the extracted macropore network the limit between micro- and macroporosity was set to the μ-CT resolution. Considering the outcrop carbonates, studied subvolumes are representative of the entire sample as parameters deduced from the 3D images are close to the MICP data. In the case of the reservoir sample, total porosity of the subvolume deduced by μ-CT is slightly higher than the one obtained by MICP, although macroporosity is identical. Thus, the difference is due to the microporous phase that is more porous in this subvolume than in the entire volume.

Table 3 gives information on the number of pores and throats as well as the average coordination number of each of the tree samples. Although the size is identical for the three samples ($1,000^3\ \mu\mathrm{m}^3$), pore and throat density is slightly higher for the reservoir carbonate than for the outcrop carbonates. Coordination numbers of the three samples are relatively close. In addition, we show the average radius of the inscribed spheres in the throat restrictions and average radius of equivalent spheres having the same volume as the pores. As can be seen, average pore sizes of the three samples have the same order of magnitude, whereas throats of the reservoir carbonate are smaller than those of the outcrop carbonates.

3.2 Pore Network Modelling: Calculation of the Petrophysical Parameters

3.2.1 Network Invasion Methodology and Wetting Films

We assume low capillary numbers, thus two-phase flow in the network follows a quasi-static displacement. Fluid distributions are then determined by simulating an invasion-percolation

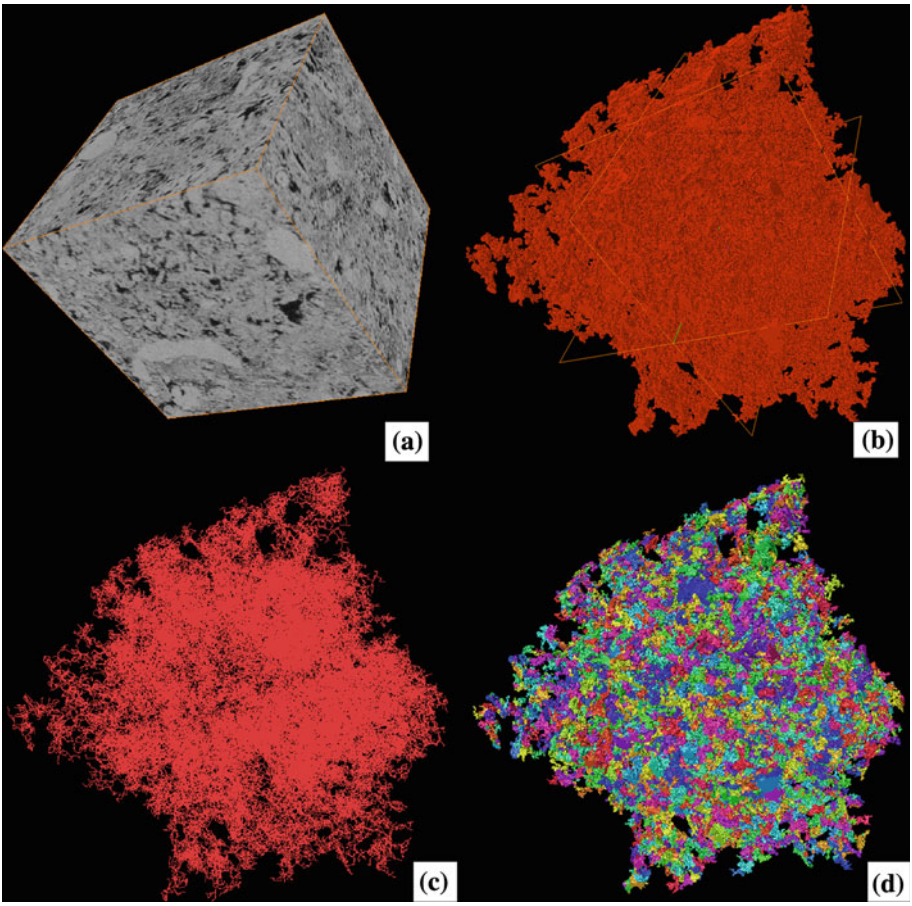

Fig. 3 Extraction of the equivalent macropore network illustrated on the reservoir sample. Original 1,000×1,000×1,000 voxel grey level image (**a**), binary image of the resolved pore space (**b**), skeleton extracted from the binary image (**c**), and partitioned macropore space (**d**)

Table 2 Data extracted from the 3D images and from the mercury intrusion experiments, ϕ: total flow porosity obtained from MICP, ϕ_{ma}: porosity obtained from MICP using the μ-CT resolution as limit between micro- and macroporosity, F_{ma}: fraction of the macroporous phase (resolved porosity), F_{mi}: fraction of the microporous phase, ϕ_{mi}: porosity of the microporous phase, F_{surf} : fraction of the macropore surface in contact with the microporous phase

Sample	MICP ϕ(%)	MICP ϕ_{ma}(%)	ϕ_{img}(%)	$\phi_{ma} = F_{ma}$ (%)	F_{mi} (%)	ϕ_{mi} (%)	F_{surf}
Reservoir	20.6	10.3	26.8	10.3	68	24	0.84
Estaillades	25	15.0	26	15.3	29	36	0.47
Lavoux	29	10.3	30	11.6	63	28	0.78

process based on the Young–Laplace equation. Further information can be found in Laroche and Vizika (2005). After the invasion of a network element (pore or throat), the area of the remaining wetting films is given by (Hui and Blunt 2000)

Table 3 Details of the pore network obtained after the extraction step

Sample	Number of pores	Number of throats	Average radius of the inscribed sphere in the throat restriction (μm)	Average radius of equivalent spheres having the same volume as pores (μm)	Average coordination number
Reservoir	15831	27849	2.6	27.7	3.52
Estaillades	11035	21455	8.6	32.9	3.88
Lavoux	11541	20073	6.7	26.7	3.47

$$A_{\mathrm{w}} = n_{\mathrm{c}}\rho^2[\cos\theta\,(\cot\alpha\cos\theta - \sin\theta) + \theta + \alpha - \pi/2], \tag{6}$$

where n_{c} represents the number of corners, α is the half angle of the polygon, θ the contact angle, and ρ the radius of the curvature of the interface between the two fluids.

3.2.2 Determination of the Intrinsic Rock Properties

The intrinsic permeability K of the network is obtained from Darcy's law at complete saturation. Flow is simulated by applying a macroscopic pressure difference ΔP across the network. The local flow rate between the pore i and the neighboring pore j is defined by Poiseuilles law

$$q_{ij} = \frac{\pi r_{\mathrm{h}}^4}{8\mu l_{\mathrm{h}}}\left(P_i - P_j\right), \tag{7}$$

where l_{h} is the hydraulic length, r_{h} the hydraulic radius, and μ the viscosity of the fluid. In each pore i mass conservation is imposed. The problem is reduced to a system of linear algebraic equations, the solution of which gives the pressure in the pores. Then the macroscopic flow rate Q can be calculated to determine the intrinsic permeability.

The analogy to the intrinsic permeability is the formation factor $\mathrm{FF} = R_0/R_{\mathrm{w}}$. To determine R_0, we apply a voltage difference ΔU across the borders of the network that induces the total current intensity I. I is then determined by solving for the electrical potential U_i in each node related to the individual electrical current in throats I_{ij} by

$$I_{ij} = \sigma_{\mathrm{w}} A_{\mathrm{w,s}}/l_{\mathrm{ff}}\left(U_i - U_j\right). \tag{8}$$

$A_{\mathrm{w,s}}$ represents the cross-sectional area occupied by the water phase (bulk or film), l_{ff} the equivalent electrical segment length (see Sect. 3.2.3) and σ_{w} the electrical conductivity of bulk water.

Once the total current I is calculated, the network resistivity corresponding to R_0 is determined by Ohm's law

$$R_0 = \frac{A\Delta U}{IL}, \tag{9}$$

where A is the network cross-section and L its length.

3.2.3 Equivalent Hydraulic and Electrical Length and Hydraulic Radius

Bauer et al. (2011) have shown that best results in terms of intrinsic permeability and formation factor were obtained when using an equivalent hydraulic (electrical) throat length l_{h} (l_{ff})

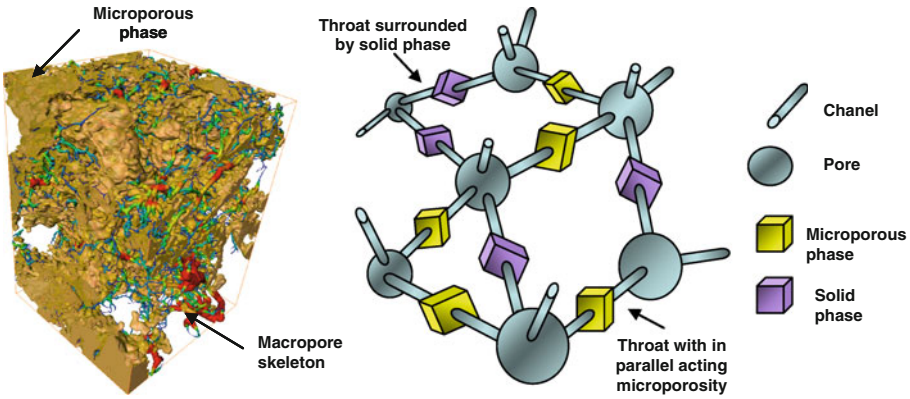

Fig. 4 Description of the matrix surrounding the throats corresponding to the macroporosity (*left* macropores surrounded by either microporous or solid phase, *right* corresponding microporosity distribution in the D-PNM)

and the hydraulic radius in Eq. 3. l_h takes into account the fact that the pressure gradient is not constant in space along the throat due to its converging and diverging shape. r_h is based on the ratio of the throat surface and its perimeter.

3.2.4 Relative Permeability and Resistivity Index Calculation

The two-phase relative permeability curves are calculated at each saturation state of the two-phase quasi-static displacements once the capillary equilibrium is reached. Identical to the one-phase flow, flow rate of the fluid α (bulk or film) in each segment is given by:

$$q_{ij}^{\alpha} = g_{h,ij}^{\alpha} \left(P_i^{\alpha} - P_j^{\alpha} \right), \tag{10}$$

where P^{α} stands for the pressure of phase α and $g_{\mathrm{h},ij}^{\alpha}$ for its conductance. For more information on $g_{\mathrm{h},ij}^{\alpha}$ we refer to Laroche et al. (1999). Relative permeabilities can be determined from the macroscopic flow rate Q_α of the phase α by:

$$K_{\mathrm{r}\alpha} = \frac{Q_\alpha \mu_\alpha L}{AK\Delta P}, \tag{11}$$

where μ_α is the viscosity of the latter.

Identical to the relative permeabilities, the electrical resistivity index $\mathrm{RI} = \frac{R_\mathrm{t}}{R_0}$ is based on the determination of the electrical resistivity R_t of the partially saturated porous media. To obtain R_t the total current intensity is calculated. To this goal, local currents are determined from Eq. 8 by correctly adapting the cross-sectional area $A_{\mathrm{w,s}}$ occupied by the water phase.

3.2.5 Dual Pore Network

The dual network model combines transport properties of the microporosity with the single pore network modeling approach applied to the interconnected macropore network. Both porosity types are supposed to act electrically and hydrodynamically in parallel. Thus, we consider two parallel networks, connected at the nodes, where the fluid exchange takes place. The first one is given by the macropore network, whereas the second one represents the macroscopic transport properties of the microporous phase (cf. Fig. 4).

The electrical conductance of the microporous phase $g_{e,mi}(S_{w,mi}(P_c))$, depending on the water saturation of the microporous phase, is given by:

$$g_{e,mi}\left(S_{w,mi}\left(P_c\right)\right) = \sigma_w[\mathrm{FF_{mi}RI_{mi}}\left(S_{w,mi}\left(P_c\right)\right)]^{-1}A_{con}/l_{con} \tag{12}$$

with $\mathrm{FF_{mi}} = a\phi_{mi}^{-m_{mi}}$ and $\mathrm{RI_{mi}}\left(S_{w,mi}\left(P_c\right)\right) = S_{w,mi}^{-n_{mi}}\left(P_c\right)$, where n_{mi} stands for the matrix saturation exponent and m_{mi} for the microporous phase cementation exponent. We suppose that microporosity follows the classical Archie law, commonly used for homogeneous structures as it is the case for Estaillades and Lavoux carbonate.

The hydraulic conductance $g_{h,mi}(S_{w,mi}(P_c))$, also depending on the water saturation, is obtained from relative permeability functions. It becomes:

$$g_{hw,mi}\left(S_{w,mi}\left(P_c\right)\right) = K_{mi}K_{rw,mi}\left(S_{w,mi}\left(P_c\right)\right)A_{con}/l_{con} \tag{13}$$

for the wetting phase and

$$g_{hnw,mi}\left(S_{w,mi}\left(P_c\right)\right) = K_{mi}K_{rw,mi}\left(1 - S_{w,mi}\left(P_c\right)\right)A_{con}/l_{con} \tag{14}$$

for the non-wetting phase. K_{mi} stands for the absolute permeability of the microporous phase.

$A_{con}l_{con}$ is the volume of microporosity surrounding a macropore segment. For further information on the influence of A_{con}/l_{con} on the transport properties we refer to Bauer et al. (2011).

3.2.6 Parameter Determination

To perform physically meaningful simulations using D-PNM, first of all, model parameters have to be determined by either experimental or numerical results or data from the μ-CT.

As described above macropores are partially surrounded by a microporous phase. The contact surface F_{surf} between micro- and macroporosity deduced from the images is transformed in a discrete number of macropore segments with microporosity acting in parallel (cf. Fig. 4). These pore segments are randomly chosen. We define p_{seg} as the percentage of macropore segments with microporosity acting in parallel. Porosity of the microporous phase ϕ_{mi} is obtained from Eq. 5. The oil/water capillary pressure of the microporous phase $P_{c,oil/water,mi}$ was calculated from the mercury injection curve assuming that all pores smaller than the μ-CT resolution belong to the microporous phase. The microporous phase cementation and saturation exponents were set to $m_{mi} = 2$ and $n_{mi} = 2$ corresponding to the classical Archie exponents. Permeability of the microporous phase of the reservoir sample was set to $K_{mi} = 8$ mD corresponding to the permeability of an oolitic microporous matrix (Zinszner and Pellerin 2007), having a pore access diameter distribution identical to the one of the microporous phase of the reservoir sample.

Relative permeability curves of the microporous phase were obtained by a single PNM simulation of a volume from the same reservoir formation solely consisting of microporous phase identical to the one of the investigated volume. As pore sizes are below the μ-CT resolution, images do not provide information on the network topology. As an approximation, a cubic network is used. Cubic networks estimate well petrophysical two-phase behavior of single porosity rocks, provided that intrinsic transport properties and throat- and pore-size distributions used in the single PNM correspond to the one of the real rock (Laroche and Vizika 2005). By fitting ϕ_{mi}, K_{mi}, $\mathrm{FF_{mi}} = \phi_{mi}^{-2}$, $P_{c,oil/water,mi}$, this requirement is achieved, and the influence of the network topology on the transport is taken into account by the intrinsic properties. However, if the latter are not available, more complex network structures should be used (Arns et al. 2004a,b) to obtain the correct macroscopic transport.

Table 4 Petrophysical parameters of the microporosity used for D-PNM simulations

	m_{mi}	n_{mi}	p_{seg}	K_{mi}	ϕ_{mi} (%)	K_{rmi}
Estaillades	2	2	0.56	–	36	–
Lavoux	2	2	0.78	–	28	–
Reservoir carbonate	2	2	0.84	8 mD	24	Single PNM simulation

Table 5 Numerical data obtained by D-PNM compared to experimental data

Sample	Estaillades exp	Estaillades num	Lavoux exp	Lavoux num	Reservoir exp	Reservoir num
FF (–)	24 ± 0.24	40.1	13 ± 0.13	29.7	50 ± 0.5	41.8 (run 1)
						42.1 (run 2)
K (mD)	273 ± 16.4	258	90 ± 5.4	133	23 ± 1.4	19.8 (run 1)
						14.2 (run 2)

We then compute relative permeabilities of the microporosity. Table 4 summarizes all the parameters used to describe the microporous phase of the different samples.

4 Results

In this section, we first use D-PNM to simulate the intrinsic as well as the electrical two-phase transport properties of the outcrop samples. Then, intrinsic transport properties and relative permeability curves of the reservoir sample will be presented.

4.1 Electrical Transport Properties

This part is principally dedicated to the evaluation of the performance of D-PNM. Indeed, a good model to simulate petrophysical transport properties should not only reproduce the classically observed Archie behavior, but also non-Archie curves. To this goal, we simulate resistivity index curves of the outcrop carbonates. As we have seen the two samples show very distinct electrical behaviors that can be explained by their different structure. Thus, the reproduction of resistivity index curves gives important information on the fact whether the model correctly takes into account the rock structure and hence on the performance of the model. The following results were obtained.

4.1.1 Estaillades Carbonate

In this carbonate, the fraction of the macropore surface in contact with the microporous phase is low. The best fit to the experimental data is found to be $p_{seg} = 0.56$ (Bauer et al. 2011). This value can be compared to $F_{surf} = 0.47$ for this carbonate.

For $p_{seg} = 0.56$ the numerical value of the formation factor is FF $= 40.12$(FF$_{exp} = 24 \pm 0.24$) and of the permeability it is $K = 258$ mD($K_{exp} = 273 \pm 16.4$ mD, see Table 5). In both cases, we obtain numerical values that have the same order of magnitude as the experimental data although values of the formation factor are not in the range of the experimental error. This deviation can probably be explained by the fact that experimental data

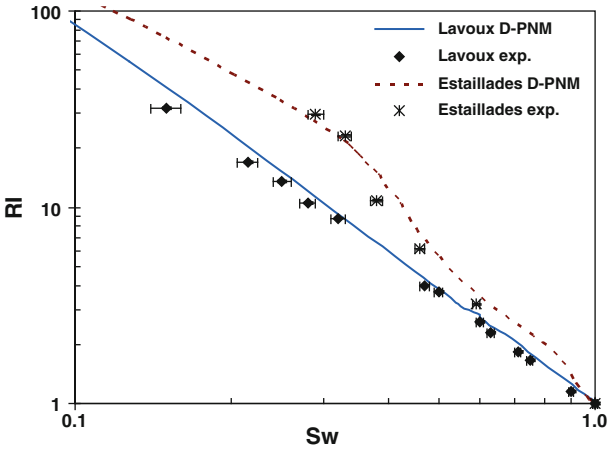

Fig. 5 Resistivity index curve of the Estaillades and Lavoux carbonate, numerical and experimental data. The experimental error of the resistance measurement is estimated to about 1% whereas the one of the saturation corresponds to 1 saturation unit

is obtained on a core whereas the network for D-PNM was reconstructed on a smaller subvolume. Already small fluctuations in heterogeneity of the subvolume compared to the core can explain this difference between experimental and numerical data. As measurements of the formation factor have low error in comparison to permeability measurements, differences due to heterogeneity are not equal to the experimental uncertainty as it is the case for the permeability. Also, a certain incertitude in the assignment of the pore and throat conductances exists.

Figure 5 shows the RI–S_w curves (numerical results and experimental data including the estimated experimental error on the saturation and the resistivity measurement). Numerical results are in relatively good accordance with the experimental results, although results are not in the range of the error bars of the experiment. The difference can be explained in the assignment of the position of macropores surrounded by microporosity as well as by the heterogeneity of the subvolume. However, most important, we can state that the experimentally observed double curvature is numerically estimated. Thus, the type of electrical transport behavior (non-Archie in this case) is correctly estimated. The double curvature can then be explained as follows. For high wetting phase saturations ($S_w \geq 0.4$) a percolating path with a relatively high conductance of the wetting phase still exists. In this saturation range, percolation is either provided by the macropores or the microporous phase. For intermediate wetting phase saturations ($0.3 < S_w < 0.4$), the percolation of the wetting phase is only provided by the remaining water films lining the macropores. Thus, the important change in the RI curvature results from the fact that the resistivity is dominated by the remaining water film.

4.1.2 Lavoux Carbonate

For this type of carbonate, we use a p_{seg} value equal to $F_{surf} = 0.78$ and we obtained FF $= 29.75$ ($FF_{exp} = 13 \pm 0.13$) and $K = 133\,\text{mD}$ ($K_{exp} = 90 \pm 5.4\,\text{mD}$). As it is the case for the Estaillades carbonate, experimental and numerical data have the same order of magnitude, differences can be explained by the heterogeneity of the subvolume used for the

reconstruction of the D-PNM and by the above mentioned uncertainty in the assignment of the pore and throat conductances.

Figure 5 shows the RI curves (numerical results for $p_{seg} = 0.78$ and experimental data). Good agreement between experimental and numerical data, especially in the high water saturation range, can be observed. For lower saturation values, numerical results follow the classical Archie behavior with a saturation exponent close to 2, whereas a slight downwards deviation can be observed in the experimental data. This difference can be probably explained by a slight difference in film size present in the macropores [see Bauer et al. (2011) for more information on the influence of the film size on the shape of the RI curves].

In summary, considering the resistivity index curves, D-PNM correctly estimates Archie (Lavoux) as well as non-Archie (Estaillades) behavior. Indeed, the shape of the resistivity index curve reflects the percolation or disconnectedness of the different water fractions (Montaron 2009), e.g., macropores and particularly microporosity. "Connectedness" of the latter is simulated in the model by p_{seg}. We have shown that by choosing values of p_{seg} close to values of F_{surf} measured on the images the shape of the resistivity index curve can be correctly estimated. Thus, the introduction of p_{seg} in the model allows the prediction of Archie or non-Archie behavior.

4.2 Relative Permeabilities

4.2.1 Reservoir Carbonate

We have seen in Sect. 3.1.3 that, if the minimal pore access diameter d_{am} given by the pore size distribution is slightly smaller than the μ-CT resolution, a connected network can still be extracted by benefitting from the heterogeneity of the sample. Permeability of the macropore network of the subsample might be higher (for identical porosity) than the one of the macropore network characterized by d_{am} of the entire sample. Simulations can still be performed; however, the macropore network has to be adapted to obtain results in accordance with the experimental data. The major interest in this part is therefore to show how to deal with this deficiency.

For this sample p_{seg} was fixed to 0.84 and we obtained $FF = 41.87 (FF_{exp} = 50 \pm 0.5)$ and $K = 19.8 (K_{exp} = 23 \pm 1.4\,\text{mD})$. Good accordance with experimental data is achieved. Figure 6 (run 1) shows the relative permeabilities during primary drainage conditions obtained with the D-PNM using the initial macropore network from Sect. 3.1.3 without modification as well as the experimental data including the estimated error in saturation determination and permeability measurement. For the wetting fluid, the agreement with the experimental curve is good, numerical results are inside the uncertainty of the experimental data, although values of the numerical relative permeabilities are slightly higher than those of the experimental relative permeabilities. This can be explained by the different injection conditions. Experimentally, relative permeabilities were obtained by injecting both fluids simultaneously (steady state, cf. 2.2.2) in the porous medium saturated by the wetting fluid. In contrast to that PNM simulates the injection of the non-wetting fluid in the network saturated by the wetting phase. This difference in injection leads to a slightly different phase distribution explaining the difference between the numerical and experimental relative permeabilities.

The relative permeability curve of the non-wetting fluid is well described for $S_w < 0.5$ and $S_w > 0.75$. However, for $0.5 < S_w < 0.75$, numerical results differ from the experimental data. The "bump" of the numerical permeability observed for $S_w \sim 0.7$ can be explained by the choice of the subvolume and the fact that permeability of its macropore

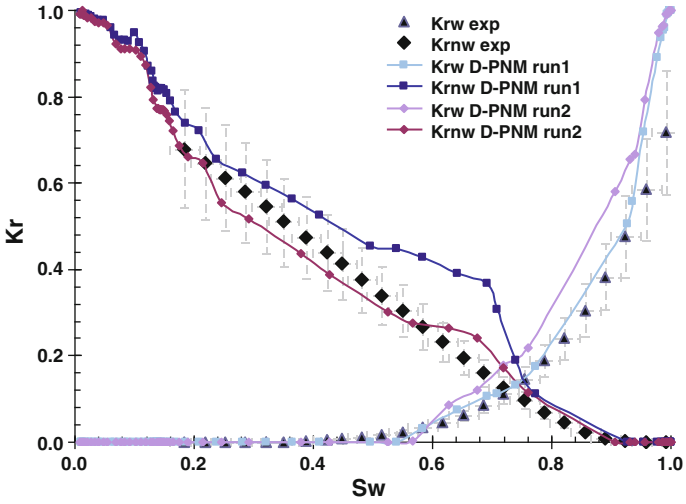

Fig. 6 Relative permeability curves of the reservoir carbonate during primary drainage conditions, run 1: initial macropore network, run2: initial macropore network with throat radii decreased by 15%

network is higher than the one of the entire sample although volume fractions of macropores are identical. Consequently, numerical oil relative permeabilities increase more rapidly than the experimental relative permeability. To overcome this deficiency throat radii of the initial macropore network were decreased until both curves (K_{rw} and K_{rnw}) were inside or very close to the experimental error bars. This was achieved by decreasing throat radii by 15%. To keep the porosity constant, the decrease in throat volume was counterbalanced by an increase in pore volume. Intrinsic transport properties become now: FF = 42.09 and $K = 14.17$, both results are still in the range of the experimental data. Relative permeabilities are given in Fig. 6 (run 2). As can be seen the "bump" in the oil permeability decreases and the agreement with the experimental curve is enhanced. Nevertheless, a slight increase of the water permeability can be observed. This is due to the fact that the total water permeability is composed of the permeability of the macropores and the one of the microporous phase. Decreasing the permeability of the macropores while keeping permeability of the microporous phase constant leads to higher values of K_{rw} in run 2 than in run 1 once the oil invasion started.

Summarizing, by decreasing the throat radii, the D-PNM approach allows treating double porosity systems with d_{am} smaller than the μ-CT resolution. However, this procedure remains arbitrary. Future study would be necessary, taking into account the fact that microporosity is not always acting in parallel to the macroporous network. This study might therefore consist in the addition of microporous zones, whose position is obtained from the μ-CT images, acting in series to the macropores. In this way, decreasing the throat radii does not implicitly lead to an increase in water permeability. In addition, it would be worth developing an image-based method combined with MICP data to determine the decrease in throat radii.

Besides a sensitivity analysis has been performed on the influence of the choice of K_{mi} on the macroscopic absolute and relative permeabilities. To this goal additional simulations were done using the macropore network of run 2 with $K_{mi} = 6$ mD and $K_{mi} = 10$ mD. We obtained the following results for the absolute permeability: $K = 12.35$ mD for $K_{mi} = 6$ mD and $K = 15.86$ mD for $K_{mi} = 10$ mD. Relative permeability curves are shown in Fig. 7. Increase or decrease of K_{mi} of 33% leads to a variation of absolute permeability of 12% and

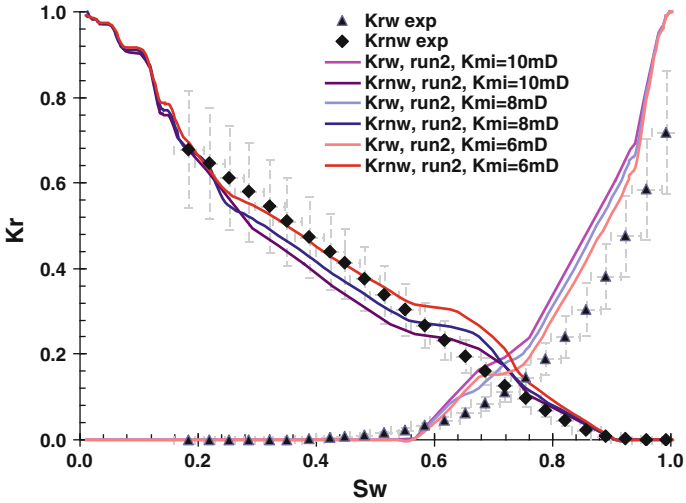

Fig. 7 Relative permeability curves of the reservoir carbonate during primary drainage conditions, experimental and numerical results using the macroporosity network for run 2 for different values of the microporosity permeability ($K_{\mathrm{mi}} = 10\,\mathrm{mD}$, $K_{\mathrm{mi}} = 8\,\mathrm{mD}$, $K_{\mathrm{mi}} = 6\,\mathrm{mD}$)

a maximal difference in relative permeability of about 15%. Thus, even though the model is sensitive to parameter values of the microporous phase, their influence remains in the experimental error range.

5 Conclusions

A general methodology to estimate the petrophysical transport behavior of carbonates characterized by a bimodal pore size distribution was presented. The method is based on the combination of high resolution μ-CT images with a Dual PNM approach. An equivalent pore network is built based on the resolved pore space obtained from the 3D images and the network parameters are extracted. A separate description of macroporosity and microporosity is done and the amount of macropore surfaces in contact with the microporous phase is determined, a useful quantity characterizing the link between these two pore systems. Then, microporosity is modeled as a parallel circuit located along the macropore throats. A principal characteristic of the model is the fraction of throats (segments) p_{seg} in which microporosity is present.

Formation factors and resistivity indices of two very distinct outcrop carbonates were simulated and compared to measurements. The experimentally observed Archie and non-Archie behavior were correctly estimated, indicating that the model has the appropriate flexibility to simulate different physical phenomena.

A major difficulty in the application of PNM to double porosity rocks lies in the requirement of the connected macropore network. This requirement is only achieved when the abscissa of the minimum between the two peaks of the pore size distribution (standing for the smallest pore access diameter of the macropores d_{am}) is higher or equal to μ-CT resolution. However, in carbonates this might not always be the case. We have shown that if d_{am} is slightly smaller than the μ-CT resolution, a connected network can still be extracted

by benefitting from the heterogeneity of the rock. Throat sizes of this network can then be adapted to estimate the experimental data. A future study will consist the development of an image-based technique in combination with MICP data to correctly adapt throat sizes for samples with d_{am} smaller than the μ-CT resolution. The addition of microporous zones, acting in series with the macropores might probably also improve the quality of the model. Real locations of the microporous zones could be deduced from the μ-CT images.

References

Adler, P.M., Thovert, J.F.: Real porous media: local geometry and macroscopic properties. Appl. Mech. Rev. **51**, 537–585 (1998)

Archie, G.E.: The electrical resistivity log as an aid in determining some reservoir characteristics. Pet. Trans. AIME **146**, 54–62 (1942)

Arns, C.H., Knackstedt, M.A., Pinczewski, W.V., Martys, N.S.: Virtual permeametry on microtomographic images. J. Pet. Sci. Eng. **45**, 41–46 (2004a)

Arns, J.Y., Robins, V., Sheppard, A.P., Sok, R.M., Pinczewski, W.V., Knackstedt, M.A.: Effect of network topology on relative permeability. Transp. Porous Media **55**, 21–46 (2004b)

Bauer, D., Youssef, S., Han, M., Bekri, S., Rosenberg, E., Fleury, M., Vizika, O.: From computed micro-tomography images to resistivity index calculations of heterogeneous carbonates using a dual-porosity pore-network approach: influence of percolation on the electrical transport properties. Phys. Rev. E **84**, 011133 (2011)

Bauget, F., Arns, C.H., Saadatfar, M., Turner, M.L., Sheppard, A.P., Sok, R.M., Pinczewski, W.V., Knackstedt, M.A.: Rock typing and petrophysical property estimation via direct analysis on microtomographic images. Paper presented at the international symposim of the society of core analysts, Toronto (2005)

Bekri, S., Laroche, C., Vizika, O.: Pore-network models to calculate transport properties in homogeneous and heterogeneous porous media. Paper presented at the computational methods in water resources XIV, Delft (2002)

Bekri, S., Howard, J., Muller, J., Adler, P.M.: Electrical resistivity index in multiphase flow through porous media. Transp. Porous Media **51**, 41–65 (2003)

Bekri, S., Laroche, C., Vizika, O.: Pore network models to calculate transport and electrical properties of single or dual-porosity rocks. Paper presented at the international symposium of the society of core analysts, Toronto (2005)

Blunt, M.J., King, P.: Macroscopic parameters from simulations of pore scale flow. Phys. Rev. A **42**, 4780–4787 (1990)

Bouvier, L., Maquignon, S.: Reconciliation of log and laboratory derived irreductible water saturation in double porosity reservoir. Advances in Core Evaluation II: Reservoir Appraisal (1991)

Caty, O., Maire, E., Youssef, S., Bouchet, R.: Modeling the properties of closed-cell cellular materials from tomography images using finite shell elements. Acta Mater. **56**, 5524–5534 (2008)

Coles, M.E., Hazlett, R.D., Spanne, P., Muegge, E.L., Furr, M.J.: Characterisation of reservoir core using computed microtomography. SPE J. **1**, 295–301 (1996)

Diaz, C.E., Chatzis, I., Dullien, F.A.L.: Simulation of capillary pressure curves using bond correlated site percolation on a simple cubic network. Transp. Porous Media **2**, 215–240 (1987)

Fatt, I.: The network model of porous media. Pet. Trans. AIME **207**, 144–163 (1956)

Fleury, M.: FRIM: A fast resistivity index measurment method. Paper presented at the international symposium of the society of core analysts, The Hague (1998)

Fleury, M.: Resistivity in carbonates: new insights. Paper presented at the SPE/ATCE, San Antonio, TX (2002)

Focke, J.W., Munn, D.: Cementation exponents in Middle Eastern carbonate reservoirs. SPE Form. Eval. **2**, 155–167 (1987)

Han, M., Youssef, S., Rosenberg, E., Fleury, M., Levitz, P.: Deviation from Archie's law in partially saturated porous media: wetting film versus disconnectedness of the conducting phase. Phys. Rev. E **79**, 031127 (2009)

Hui, M.H., Blunt, M.J.: Effects of wettability on three-phase flow in porous media. J. Phys. Chem. B **104**, 3833–3845 (2000)

Ioannidis, M.A., Chatzis, I.: A dual-network model of pore structure for vuggy carbonates. Paper presented at the international symposium of the society of core analysts, Abu Dhabi (2000)

Knackstedt, M.A., Arns, C.H., Limaye, A., Arns, C.H., Limaye, A., Sakellariou, A., Senden, T.J., Sheppard, A.P., Sok, R.M., Pinczewski, W.V., Bunn, G.F.: Digital core laboratory: reservoir-core properties derived from 3D images. J. Pet. Technol. **56**, 66–68 (2004)

Knackstedt, M.A., Arns, C.H., Ghous, A., Sakellariou, A., Senden, T.J., Sheppard, A.P., Sok, R.M., Averdunk, H., Pinczewski, W.V., Padhy, G.S., Ioannidis, M.A.: 3D imaging and flow characterisation of the pore space of carbonate core samples. Paper presented at the international symposium of the society of core analysts, Trondheim (2006)

Knackstedt, M.A., Arns, C.H., Sheppard, A.P., Senden, T.J., Sok, R.M., Cinar, Y., Olafuyi, A.O., Pinczewski, W.V., Padhy, G.S., Ioannidis, M.A.: Pore scale analysis of electrical resistivity in complex core material. Paper presented at the international symposium of the society of core analysts, Calgary (2007)

Laroche, C., Vizika, O.: Two-phase flow properties prediction from small-scale data using pore-network modeling. Transp. Porous Media **61**, 77–91 (2005)

Laroche, C., Vizika, O., Kalaydjian, F.: Network modeling as a tool to predict three-phase gas injection in heterogeneous wettability porous media. J. Pet. Sci. Eng. **24**, 155–168 (1999)

Lenormand, R., Zarcone, C., Sarr, A.: Mechanisms of the displacement of one fluid by another in a network of capillary ducts. J. Fluid Mech. **135**, 337–353 (1983)

Lindquist, W.B., Venkatarangan, A., Dunsmuir, J., Wong, T.F.: Pore and throat size distributions measured from synchrotron X-ray tomographic images of Fontainebleau sandstones. J. Geophys. Res. Solid Earth **105**, 21509–21527 (2000)

Moctezuma-Berthier, A., Bekri, S., Laroche, C., Vizika, O.: A dual network model for relative permeability of bimodal rocks: application in a vuggy carbonate. Paper presented at the international symposium of the society of core analysts, Pau (2003)

Montaron, B.: Connectivity theory–a new approach to modeling non-Archie rocks. Petrophysics **50**, 102–115 (2009)

Olafuyi, A.O., Cinar, Y., Knackstedt, M.A., Pinczewski, W.V.: Capillary pressure and relative permeability of small cores. Paper presented at the SPE/DOE improved oil recovery symposium, Tulsa, OK (2008)

Oren, P.E., Bakke, S., Arntzen, O.J.: Extending predictive capabilities to network models. SPE J. **3**, 324–336 (1998)

Padhy, G.S., Ioannidis, M.A., Lemaire, C., Coniglio, M.: Mesurement and interpretation of non-Archie resistivity behavior in model and real vuggy carbonates. Paper presented at the international symposium of the society of core analysts, Trondheim (2006)

Patzek, T.W., Silin, D.B.: Shape factor and hydraulic conductance in noncircular capillaries I. One-phase creeping flow. J. Colloid Interface Sci. **236**, 295–304 (2001)

Payatakes, A.C., Tien, C., Turian, R.M.: A new model for granular porous media: part I. Model formulation. Aiche J. **19**, 58–67 (1973)

Pudney, C.: Distance-ordered homotopic thinning: a skeletonization algorithm for 3D digital images. Comput. Vis. Image Underst. **72**, 404–413 (1998)

Schlumberger, I.: Log interpretation: principles/application. Schlumberger Educational Services, Houston, TX (1987)

Sholokhova, Y., Kim, D., Lindquist, W.B.: Network flow modeling via lattice-Boltzmann based channel conductance. Adv. Water Resour. **32**, 205–212 (2009)

Valvatne, P.H., Blunt, M.J.: Predictive pore-scale network modeling. Paper presented at the SPE/ATCE, Denver, CO (2003)

Youssef, S., Han, M., Bauer, D., Rosenberg, E., Bekri, S., Fleury, M., Vizika, O.: High resolution μ-CT combined to numerical models to assess electrical properties of bimodal carbonates. Paper presented at the international symposium of the society of core analysts, Abu Dhabi (2008)

Zinszner, B., Pellerin, F.M.: Geoscientist's guide to petrophysics. Technip (2007)